Role of specific distorted metal complexes in exciton self-trapping for hybrid metal halides

Romain Gautier, Rodolphe Clérac, Michaël Paris, Florian Massuyeau

Role of specific distorted metal complexes in exciton self-trapping for hybrid metal halides†

Romain Gautier, *[a] Rodolphe Clérac, [b] Michael Paris [a] and Florian Massuyeau[a]

A methodology enabling the discovery of hybrid metal halide phosphors through the selection of structural networks, which exhibit a specific distorted environment of the metal ions associated with the self-trapping of excitons, is proposed. This approach is demonstrated with the synthesis of an efficient near-UV emitting hybrid cadmium halide phosphor.

Owing to the emergence of the low-dimensional hybrid perovskites as materials for optoelectronics, metal halides have recently been at the center of new attention.[1,2] Thus, in addition to the promising photovoltaic applications, these compounds exhibit tunable photoluminescence properties which make them interesting candidates for light emitting diode (LED) applications. Recently, the synthesis of efficient broadband emitting hybrid metal halides for solid-state lighting (SSL) has been reported.[3–17] Such emission is often attributed to the self-trapping of excitons (STE) as previously reported in the binary metal halides such as KX, PbX_2, or CdX_2, (X = halides).[18] In these binary materials, the STE is commonly associated with a distortion in the metal ion coordination sphere.[19–22] For example, in cadmium halide binary compounds, the STE was previously described as a deformation of CdX_6 sites which would be similar to the inherent distortion of $Cu^{II}X_6$ moieties.[23] In addition, Wang *et al.* recently revealed that an STE with Jahn–Teller-like octahedral distortion would be mainly responsible of the broadband emissions observed in hybrid metal halides.[22] In this context, we investigated the synthesis of cadmium and copper halides based on *trans*-2,5-dimethylpiperazine (abbreviated TDMP in the following) to unravel the relationships between ground-state distortion and STE. The present work suggests that the future discoveries of efficient hybrid metal halide phosphors could be facilitated by studying the photoluminescence properties of known materials exhibiting specific distortions.

The syntheses of the two hybrid metal halide compounds were carried out under hydrothermal conditions from mixtures of metals, HCl and *trans*-2,5-dimethylpiperazine (ESI†). A new compound based on Cd(II) isostructural to the previously reported Cu(II) compound (bond valence calculations: 1.72 v.u. and 1.85 v.u. for Cu and Cd, respectively) was isolated (Fig. S1, ESI†) and the structure was determined by single-crystal X-ray diffraction (Tables S1–S4, ESI†).[24] The presence of *trans*-2,5-dimethylpiperazine-1,4-diium cations ($TDMP^{2+}$) was confirmed by the FTIR measurements (Fig. S2, ESI†). Elemental

[a] *Université de Nantes, CNRS, Institut des Matériaux Jean Rouxel, IMN, F-44000 Nantes, France. E-mail: Romain.Gautier@cnrs-imn.fr*
[b] *Univ. Bordeaux, CNRS, Centre de Recherche Paul Pascal, UMR 5031, 33600 Pessac, France*

Romain Gautier

Romain Gautier is currently a research scientist at Centre National de la Recherche Scientifique (CNRS) in the Institut des Matériaux Jean Rouxel. Prior to this position, he obtained a PhD degree from Ecole Nationale Supérieure de Chimie de Rennes in inorganic and materials chemistry in 2010. Then, he moved to Northwestern University as a postdoc in the group of Prof. Poeppelmeier. In 2019, he received the CNRS Bronze medal and the National Chinese Award of ''1000 Young Talents Program''. His current research interests include the design, synthesis and characterization of new inorganic and hybrid materials with properties of second harmonic generation and luminescence.

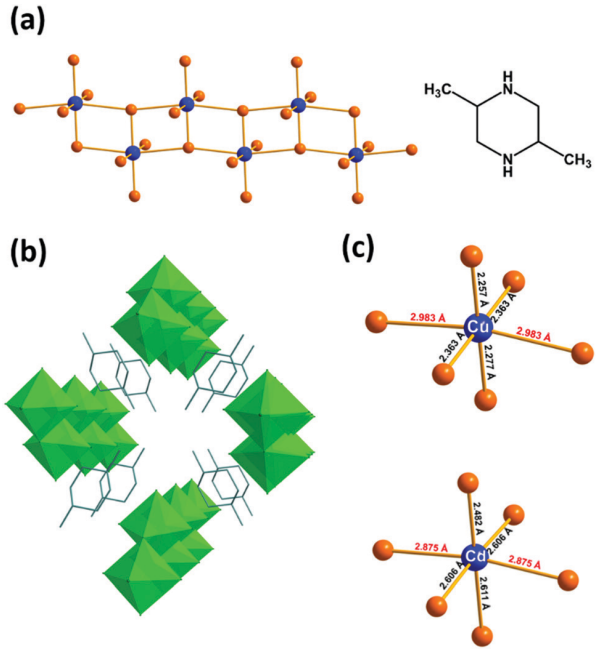

Fig. 1 Representation of (a) the ladder-type structure of copper and cadmium chloride compounds and the *trans*-2,5-dimethylpiperazine (TDMP) molecule, (b) the packing of inorganic ladders and $TDMP^{2+}$ cations and (c) the distortion of metal chloride octahedra.

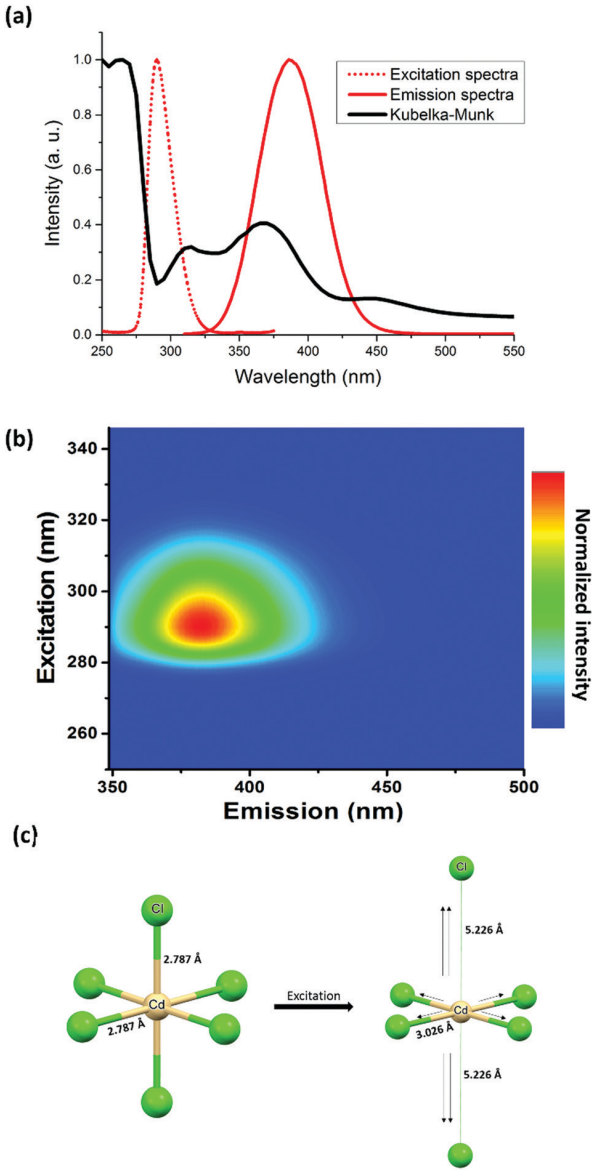

Fig. 2 (a) Absorption, excitation (λ_{em} = 385 nm), and emission (λ_{exc} = 290 nm) spectra of $(TDMP)CdCl_4$. (b) PL excitation *vs.* emission mapping of $(TDMP)CdCl_4$, and (c) calculated distortion of $[CdX_6]^{4-}$ motifs under excitation.

analysis by EDS (1/4.3 for Cu/Cl and 1/4.0 for Cd/Cl) agrees with the expected M/Cl ratios (Fig. S3, ESI†). The two isostructural materials are built with anionic metal halide ladders isolated between $TDMP^{2+}$ cations (Fig. 1a, b and Fig. S4, ESI†). Even if these two compounds $(TDMP)MCl_4$ (M = Cu or Cd) exhibit structural similarities with the previously reported $(TDMP)PbX_4$ (X = Cl, Br, I; *i.e.* ladder structures of the metal halide, same ratio TDMP/M/X, edge-sharing MX_6 units, shift between adjacent ladders...),[20,25] some major structural differences can be observed (Fig. S5, ESI†). The structure of the latter is related to the post-perovskites: the inorganic ladder is derived from the two-dimensional post-perovskite structure by slicing perpendicularly to the *a* axis and consists of both edge-sharing and corner-sharing MX_6 units. On the other hand, the $(TDMP)MCl_4$ (M = Cu or Cd) structures cannot be related to the perovskite or post-perovskite structures. In the present case, the ladder is built exclusively of edge-sharing MCl_6 octahedral units.

The ladders in $(TDMP)MCl_4$ (M = Cu or Cd) are composed of metal chloride octahedra ($2.2571(5) < d_{Cu-Cl} < 2.9834(1)$ Å for $(TDMP)CuCl_4$ and $2.4825(7) < d_{Cd-Cl} < 2.8751(1)$ Å for $(TDMP)CdCl_4$; Fig. 1c). It is important to note that a strong first-order Jahn–Teller distortion (JTD) is observed on the $CuCl_6$ octahedra motif with short and long Cu–Cl bonds perpendicular and along the ladders, respectively. More interestingly, for $(TDMP)CdCl_4$, the cadmium also exhibits a similar distorted environment with two long Cd–Cl bonds (2.8751(1) Å) along the 1D structure and four short Cd–Cl bonds ($2.4825(7)$ Å $< d_{Cd-Cl} <$ 2.6108(6) Å) perpendicular to the ladder. Thus, the four chloride ligands coordinated to one or two Cd are associated with short Cd–Cl bond lengths whereas the two other ligands, in the *trans*-position to each other, are coordinated to three Cd and are associated with the longest Cd–Cl bond lengths. In addition, the distortion of the $CdCl_6$ octahedra is detected by the notable chemical shift anisotropy extracted from the spinning side bands manifold of the ^1H–^{113}Cd CP-MAS NMR spectrum (Fig. S6, ESI†). The observation of such similar distortions (nearly D_{4h}) for both compounds shows that the inorganic network not only accommodates such inherent D_{4h} distortion of the metal complexes but is also at its origin.

Concerning the optical properties of $(TDMP)CdCl_4$, absorption peaks observed below the bandgap at about 280 nm (Fig. 2a) can

be assigned to intra-gap states. Upon excitation at 290 nm, the d^{10} Cd(II) based compound exhibits a strong emission at 385 nm (Fig. 2a, b and Fig. S7, S8, ESI†) with a high photoluminescence quantum yield (PLQY = 40%) and a relatively high thermal stability (decomposition at about 250 °C; Fig. S9, ESI†). In addition to this intense photoluminescence (PL) emission, a weak luminescence can be observed in the visible region (around 500 nm; Fig. S10, ESI†). The observed emissions exhibit important Stokes shifts together with slight blue shifts and broadenings upon heating from 77 K to room temperature. This thermal dependence is indeed typical of emissions originating from STE. In addition, the decay times of the two emissions (0.54 ns for the high energy band and 0.69 ns for the low energy band) are similar to previously reported ones in other hybrid metal halides. Similar near-UV and green-yellow emissions are also observed for CdX_2 binary compounds (X = Cl, Br, I) at low temperature,[23,26–28] and these emissions were both assigned to STE associated with a distortion of the CdX_6 units. To support such mechanism,[23,27] Nakagawa *et al.* showed that the electron paramagnetic resonance (EPR) spectra of irradiated CdX_2 crystals exhibited similar structures as the ones of Cu^{2+} or Ag^{2+} doped cadmium halide crystals. Thus, this observation suggested that the excited states of the CdX_6 units would be symmetrically similar to the inherent distortion of the Cu^{2+} based octahedral complex.

To further unravel the deformation of the inorganic lattice responsible for the STE, DFT and TDDFT calculations were carried out (see details in the ESI†). After optimizing the excited state of $[CdX_6]^{4-}$ units, a deformation corresponding to a D_{4h} distortion (lengthening of two opposite Cd–X bonds associated with the shortening of four equatorial Cd–X bonds) was observed (Fig. 2c). Interestingly, another recent theoretical investigation of the 0D lead perovskite, Cs_4PbBr_6, suggested that the STE occurs with the same distortion: shortening of four Pb–Br equatorial bonds together with the elongation of the two remaining bonds.[29] The calculation of the electronic DOS of the STE structure showed the presence inside the band gap of an unoccupied hole state (Br p + Pb s) with an occupied electron state (Pb p + Br p). In addition, the same chains have been reported for the broad-band emitters $C_4N_2H_{14}PbX_4$ (X = Cl, and Br, $C_4N_2H_{14}$ = *N*,*N*′-dimethylethylene-1,2-diammonium),[30,31] exhibiting relatively high photoluminescence quantum yields (PLQYs about 20%). Concerning the chloride analogue, Wu *et al.* proposed that the emission originates from the distortion of the six Pb–X bonds with a contraction of four planar Pb–X bonds and elongation of the two other Pb–X bonds. Following this work, Wang *et al.* performed DFT calculations on the lead bromide ladder-like chains.[31] They identified two STEs, one Jahn–Teller like (STE1) at high energy which is the most stable and one non-Jahn–Teller at lower energy (STE2). Thus, the two emissions at 385 and 500 nm for our cadmium chloride, could be related to the same mechanisms. Interestingly, the STE through a Jahn–Teller like distortion has also been reported for other metal halides such as $Cs_2AgInCl_6$ in which $AgCl_6$ distortion was shown to be responsible for highly efficient broad-band emission. Thus, this Jahn–Teller distortion could be a general phenomenon which occurs in the excited states and would be at the origin of the broadband luminescence of many metal halides.

In $(TDMP)CdCl_4$, the D_{4h} distortion of the CdX_6 units induced by the inorganic network is already observed in the ground state. Such distortion would also promote the STE and the enhancement of the associated luminescence. Thus, the intra-gap states observed in the absorption spectra (Fig. 2a) would be associated with the distorted CdX_6 units, which would behave as traps for the excitons (extrinsic self-trapping). Promoting this distortion by targeting crystal structures in which the excited states are likely to form could also be an interesting strategy to synthesize materials with enhanced photoluminescence from STE. Of particular interest, families of isostructural metal (Cu(II), Cd(II) and Pb(II)) halide materials would be interesting to explore. If the inherent Jahn–Teller distortion of the Cu(II) site is possible in a specific network, one can expect the same distortion to be possible in the excited states when considering other metal ions such as Cd(II) and Pb(II).

In addition to the specific distortion of the MX_6 octahedral units, other structural features help to assist the STE and prevent the PL quenching. Thus, similar to previously reported lead halide ladders, lowering the dimensionality lowers the deformation energy and the associated barrier to self-trapping.[18,25] This phenomenon would explain why intense STE emissions can be observed at room temperature for the 0D and 1D metal halides whereas the 2D or 3D systems such as the binary MX_2 show intense STE emission only at cryogenic temperatures. To prevent PL quenching, the organic cations should also hardly interact with the inorganic metal halide.[20] In the $(TDMP)CdCl_4$, the organic cations are favorably far from the inorganic ladders. To evaluate the organic–inorganic interactions, one can compare the bond distances of the organic molecules in the hybrid structure *vs.* the halide salt.[20] In $(TDMP)Cl_2$,[32] the C–C and C–N bond distances are very similar to the one in $(TDMP)CdCl_4$ (Table S2, ESI†). ^{13}C NMR spectroscopy is another way to check the organic–inorganic interactions. Fig. 3 shows the ^1H–^{13}C CP-MAS NMR spectrum of $(TDMP)CdCl_4$. Although a single crystallographic site was determined by X-ray diffraction, the resonances of CH_3 (15–18 ppm), CH_2 (47–50 ppm) and CH (50–53 ppm) moieties exhibit multiple lines. It is likely that the resonance splits originate from the hydrogen bond network between the organic and inorganic parts of the compound. As already described, the inorganic chains of the

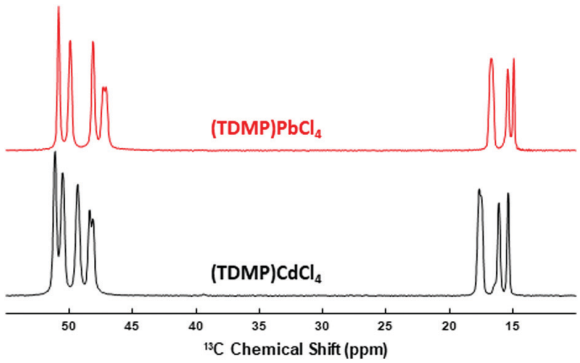

Fig. 3 ^1H–^{13}C CP-MAS NMR spectra of $(TDMP)CdCl_4$ and $(TDMP)PbCl_4$.

(TDMP)$CdCl_4$ and (TDMP)$PbCl_4$ materials differ. However, the local environment of the $TDMP^{2+}$ cations is highly similar within these two structures (Fig. S11, ESI†). This strong similarity, including the hydrogen bond network, is supported by the strong resemblance between the ^{1}H–^{13}C CP-MAS NMR spectrum of (TDMP)$CdCl_4$ and those of (TDMP)$PbCl_4$ (Fig. 3) and its bromide counterpart (TDMP)$PbBr_4$ previously reported.[33] Moreover, for this latter material, we showed that the interactions between the organic and inorganic parts are weak.[20] Hence, weak interactions between the $TDMP^{2+}$ cations and cadmium chloride ladders would prevent the PL quenching by the C–H vibration modes.[20,34,35]

In summary, a new type of cadmium halide ladder-like chain with intense photoluminescence was isolated. The one-dimensional structure as well as photoemission originating from the STE show similarities with previously reported post-perovskite related lead halide compounds. The analysis of the crystal structures and associated properties shows that the STE can be assisted by specific distortions around the metal ion. In the case of (TDMP)$CdCl_4$, the excited states would be related to the distortion of the $CdCl_6$ octahedral motif, which is similar to the inherent first-order Jahn–Teller distortion of $Cu^{II}Cl_6$ units. Such distortion can be well accommodated in this ladder-type structure as shown by the isostructural (TDMP)$CuCl_4$ that could also be prepared using the same experimental conditions. As a multitude of Cu(II) halide phases with Jahn–Teller distortion have been synthesized and thoroughly investigated in the past for their magnetic properties, a future methodology could consist of synthesizing isostructural metal (Cd(II), Pb(II)…) halides in order to directly target materials in which the STE and the associated photoluminescence would be promoted. A first approach could consist of identifying, through the use of structural databases such as the Cambridge Structural Database (CSD), previously reported hybrid metal halides (particularly Cd(II) and Pb(II) based systems) isostructural to hybrid copper(II) halides and investigate their photoluminescence properties. Such strategy could greatly accelerate the discovery of phosphors with high photoluminescence quantum yields for LED applications.

This work was supported by the CNRS, the National Agency for Research (ANR Young Researchers, ANR-16-CE08-0003-01, Combi-SSL project), the Region Pays de la Loire (Etoiles montantes en Pays de la Loire 2017, project ''Découverte de pérovskites hybrides assistée par ordinateur''), the University of Bordeaux, the Région Nouvelle Aquitaine, the MOLSPIN COST action CA15128, and the GdR MCM-2. Calculations were conducted at Centre de Calcul Intensif des Pays de la Loire, Université de Nantes. We thank Stéphane Grolleau for thermal measurements on both materials.

References

1 M. I. Saidaminov, O. F. Mohammed and O. M. Bakr, *ACS Energy Lett.*, 2017, **2**, 889–896.
2 B. Saparov and D. B. Mitzi, *Chem. Rev.*, 2016, **116**, 4558–4596.
3 A. Nagami, K. Okamura and T. Ishihara, *Phys. B*, 1996, **227**, 346–348.
4 T. Ishihara, *Optical Properties of Low-dimensional Materials*, World Scientific, 1996, pp. 288–339.
5 E. R. Dohner, E. T. Hoke and H. I. Karunadasa, *J. Am. Chem. Soc.*, 2014, **136**, 1718–1721.
6 L. Mao, Y. Wu, C. C. Stoumpos, M. R. Wasielewski and M. G. Kanatzidis, *J. Am. Chem. Soc.*, 2017, **139**, 5210–5215.
7 L. Mao, P. Guo, M. Kepenekian, I. Hadar, C. Katan, J. Even, R. D. Schaller, C. C. Stoumpos and M. G. Kanatzidis, *J. Am. Chem. Soc.*, 2018, **140**, 13078–13088.
8 R. Roccanova, M. Houck, A. Yangui, D. Han, H. Shi, Y. Wu, D. T. Glatzhofer, D. R. Powell, S. Chen, H. Fourati, A. Lusson, K. Boukheddaden, M.-H. Du and B. Saparov, *ACS Omega*, 2018, **3**, 18791–18802.
9 A. Yangui, R. Roccanova, T. M. McWhorter, Y. Wu, M.-H. Du and B. Saparov, *Chem. Mater.*, 2019, **31**, 2983–2991.
10 C. Zhou, H. Lin, Y. Tian, Z. Yuan, R. Clark, B. Chen, L. J. van de Burgt, J. C. Wang, Y. Zhou, K. Hanson, Q. J. Meisner, J. Neu, T. Besara, T. Siegrist, E. Lambers, P. Djurovich and B. Ma, *Chem. Sci.*, 2018, **9**, 586–593.
11 Y.-Y. Guo, J. A. McNulty, N. A. Mica, I. D. W. Samuel, A. M. Z. Slawin, M. Bühl and P. Lightfoot, *Chem. Commun.*, 2019, **55**, 9935–9938.
12 G. Zhou, X. Jiang, M. Molokeev, Z. Lin, J. Zhao, J. Wang and Z. Xia, *Chem. Mater.*, 2019, **31**, 5788–5795.
13 Z. Song, J. Zhao and Q. Liu, *Inorg. Chem. Front.*, 2019, **6**, 2969–3011.
14 R. Zhang, X. Mao, Y. Yang, S. Yang, W. Zhao, T. Wumaier, D. Wei, W. Deng and K. Han, *Angew. Chem., Int. Ed.*, 2019, **58**, 2725–2729.
15 G. Zhou, B. Su, J. Huang, Q. Zhang and Z. Xia, *Mater. Sci. Eng., R*, 2020, **141**, 100548.
16 G. Song, M. Li, Y. Yang, F. Liang, Q. Huang, X. Liu, P. Gong, Z. Xia and Z. Lin, *J. Phys. Chem. Lett.*, 2020, **11**, 1808–1813.
17 C. Deng, G. Zhou, D. Chen, J. Zhao, Y. Wang and Q. Liu, *J. Phys. Chem. Lett.*, 2020, **11**, 2934–2940.
18 K. S. Song and R. T. Williams, *Self-Trapped Excitons*, Springer-Verlag, Berlin Heidelberg, 1993.
19 J. Luo, X. Wang, S. Li, J. Liu, Y. Guo, G. Niu, L. Yao, Y. Fu, L. Gao, Q. Dong, C. Zhao, M. Leng, F. Ma, W. Liang, L. Wang, S. Jin, J. Han, L. Zhang, J. Etheridge, J. Wang, Y. Yan, E. H. Sargent and J. Tang, *Nature*, 2018, **563**, 541–545.
20 R. Gautier, F. Massuyeau, G. Galnon and M. Paris, *Adv. Mater.*, 2019, **31**, 1807383.
21 M.-H. Tremblay, F. Thouin, J. Leisen, J. Bacsa, A. R. Srimath Kandada, J. M. Hoffman, M. G. Kanatzidis, A. D. Mohite, C. Silva, S. Barlow and S. R. Marder, *J. Am. Chem. Soc.*, 2019, **141**, 4521–4525.
22 X. Wang, W. Meng, W. Liao, J. Wang, R.-G. Xiong and Y. Yan, *J. Phys. Chem. Lett.*, 2019, **10**, 501–506.
23 M. Kitaura, H. Nakagawa, K. Fukui, M. Fujita, T. Miyanaga and M. Watanabe, *J. Electron Spectrosc. Relat. Phenom.*, 1996, **79**, 175–178.
24 Ü. Kersen, A. Wojtczak, A. Bienko and J. Jezierska, *New J. Chem.*, 2018, **42**, 15705–15713.
25 R. Gautier, M. Paris and F. Massuyeau, *J. Am. Chem. Soc.*, 2019, **141**, 12619–12623.
26 M. Kitaura and H. Nakagawa, *J. Lumin.*, 1995, **66–67**, 438–442.
27 H. Nakagawa and M. Kitaura, *International Conference on Excitonic Processes in Condensed Matter*, International Society for Optics and Photonics, 1995, vol. 2362, pp. 294–304.
28 S. Kawabata and H. Nakagawa, *J. Lumin.*, 2007, **126**, 48–52.
29 B. Kang and K. Biswas, *J. Phys. Chem. Lett.*, 2018, **9**, 830–836.
30 Z. Yuan, C. Zhou, Y. Tian, Y. Shu, J. Messier, J. C. Wang, L. J. van de Burgt, K. Kountouriotis, Y. Xin, E. Holt, K. Schanze, R. Clark, T. Siegrist and B. Ma, *Nat. Commun.*, 2017, **8**, 14051.
31 G. Wu, C. Zhou, W. Ming, D. Han, S. Chen, D. Yang, T. Besara, J. Neu, T. Siegrist, M.-H. Du, B. Ma and A. Dong, *ACS Energy Lett.*, 2018, **3**, 1443–1449.
32 J. C. J. Bart, I. W. Bassi and R. Scordamaglia, *Acta Crystallogr., Sect. B: Struct. Crystallogr. Cryst. Chem.*, 1978, **34**, 2760–2764.
33 H. Yuan, F. Massuyeau, N. Gautier, A. B. Kama, E. Faulques, F. Chen, Q. Shen, L. Zhang, M. Paris and R. Gautier, *Angew. Chem.*, 2020, **132**, 2824–2829.
34 D. Cortecchia, J. Yin, A. Bruno, S.-Z. A. Lo, G. G. Gurzadyan, S. Mhaisalkar, J.-L. Brédas and C. Soci, *J. Mater. Chem. C*, 2017, **5**, 2771–2780.
35 A. Yangui, D. Garrot, J. S. Lauret, A. Lusson, G. Bouchez, E. Deleporte, S. Pillet, E. E. Bendeif, M. Castro, S. Triki, Y. Abid and K. Boukheddaden, *J. Phys. Chem. C*, 2015, **119**, 23638–23647.

SUPPORTING INFORMATION

Role of Specific Distorted Metal Complexes in the Exciton Self-Trapping for Hybrid Metal Halides

Romain Gautier,[a,*] *Rodolphe Clérac*[b], *Michael Paris,*[a] *Florian Massuyeau*[a]

Synthesis

The metal halide materials have been synthesized by hydrothermal methods from mixtures of the chosen metal Cu (Merck, 99.7%) or Cd (Tougart and Matignon, 99%), *trans*-2,5-dimethylpiperazine (Alfa Aesar, 98%) and HCl (Alfa Aesar, 37%). The two compounds were synthesized by mixing 500 mg of cadmium (4.4 mmol) or copper (7.9 mmol), 500 mg of *trans*-2,5-dimethylpiperazine (4.4 mmol), and 3 ml of HCl 37%. The reactants were placed in a 23 mL Teflon-lined stainless-steel autoclave, heated to 180°C during 24 hours and slowly cooled down to room temperature at the rate of 10°C/h. Single crystals or/and powders were recovered by vacuum filtration.

Structure determination

Structure determinations were carried out from single-crystal X-ray diffraction with a Bruker-Nonius Kappa CCD diffractometer with monochromated Mo Kα radiation and a crystal to detector distance of 60 mm. Absorption corrections were carried out with SADABS.[1] Direct methods were used to determine the crystal structures and were completed by Fourier difference syntheses with SIR2004.[2] The refinement of the crystal structures with anisotropic displacement parameters was carried out using SHELXL-2013.[3] The CIFs were compiled with Olex2.12.[4] Additional symmetry elements were checked with the program PLATON.[5] Crystallographic data for these compounds are summarized in table S1.

NMR spectroscopy

^{113}Cd NMR experiment was conducted on a 300 MHz (7 T) Bruker NEO spectrometer. The powder sample was packed in a 4 mm o.d. rotor. ^{1}H-^{113}Cd CP-MAS (Cross-Polarization Magic Angle Spinning) spectrum was acquired with a contact time of 2 ms. MAS frequency was set to 2.5 kHz and the recycle delay to 1 s. ^{113}Cd chemical shift is referenced to $Cd(ClO_4)_2$ at 0 ppm. 'dmfit' program was used for spectral simulation.[6]

^{13}C and ^{15}N NMR experiments were conducted on a 500 MHz (11.7 T) Bruker Avance III spectrometer. Powdered samples were packed in a 4 mm o.d. rotor. ^{1}H-^{13}C and ^{1}H-^{15}N CP-MAS spectra were acquired with a contact time of 3 ms. The recycle delay was set to 3 s for both ^{13}C and ^{15}N experiments. MAS frequency was set to 10 and 5 kHz for ^{13}C and ^{15}N spectra, respectively. ^{13}C and ^{15}N chemical shifts are referenced to TMS and NH_3, respectively.

Magnetic susceptibility measurements

The magnetic susceptibility measurements were performed on a Quantum Design SQUID MPMS-XL magnetometer housed at the Centre de Recherche Paul Pascal at temperatures between 1.8 and 400 K and *dc* magnetic fields ranging from -7 to +7 T. The measurements were carried out on polycrystalline samples (20.50 mg) introduced in a sealed polyethylene bag (typically 3 × 0.5 × 0.02 cm; 23.02 mg). Prior to the experiments, the field-dependent magnetization was measured at 100 K in order to detect the presence of any bulk ferromagnetic impurities. Paramagnetic or diamagnetic materials should exhibit a perfectly linear dependence of the magnetization that extrapolates to zero at zero *dc* field which is the case for the present sample confirming the absence of any ferromagnetic

impurities. The magnetic susceptibilities were corrected for the sample holder and the intrinsic diamagnetic contributions.

The magnetic susceptibility of (TDMP)$CuCl_4$ follows a Curie-Weiss law with an average *g* factor of 2.11(5) and a Weiss constant of -0.74(2)K indicating weak antiferromagnetic interactions between *S* = 1/2 Cu centers through the chloride bridges. A quantum *S* =1/2 spin chain model (H= -2J $\Sigma(\mathbf{S}_i \bullet \mathbf{S}_{i+1})$) was used considering only the dichloride bridges as a magnetic pathway. This model gives a remarkably good theory/experience agreement with J/k_B = -0.56(1) K (and g = 2.11(5)) (Figure S14). Even if our model is slightly different than the one previously reported by Kersen et al.,[7] the paramagnetic properties of (TDMP)$CuCl_4$ and the g (2.17) and J/k_B (-0.84 K) parameters are in good agreement.

UV/Visible and FTIR Spectroscopy

UV/Visible Spectroscopy. Diffuse reflectance spectra from 250 to 2500 nm were recorded on a Varian Cary 5G spectrophotometer using a 60 mm integrating sphere. Kubelka Munk function ($a/S = (1-R)^2/2R$ where a is the absorption coefficient, S the scattering coefficient and R the reflectance) was used to calculate absorbance from reflectance spectra.

FT-IR Spectroscopy. The materials were mixed with KBr and pressed into pellets. FT-IR spectra (100 scans) were collected with a Vertex 70 Instrument from 400 to 4000 cm^{-1} and a resolution of 4 cm^{-1}. A background spectrum was subtracted from the collected spectra.

Photoluminescence

Photoluminescence spectra were collected using a Spex Fluorolog-3 spectrofluorometer from Instruments Jobin Yvon. 450W Xe light was used as excitation source. The variations of incident lamp flux and of the response of the photomultiplier were corrected for excitation and emission spectra, respectively. Photoluminescence Quantum Yields (PLQY) measurements are relative to the PLQY of SGA 550 100 isiphor® from Sigma Aldrich (exhibiting a PLQY near 95%). Time-resolved photoluminescence (TRPL) measurements were obtained with an excitation of 267 nm provided by a regenerative amplified femtosecond Ti:Sapphire laser system (Spectra Physics Hurricane X) frequency-tripled. Transient signals were recorded by means of a streak camera Hamamatsu C7700 coupled with a SP2300 imaging Acton spectrograph from Princeton Instruments.

DFT calculations

Molecular structures were optimized using Gaussian 16 Rev. A.03 suite of programs.[8] Isolated octahedral units were optimized using DFT calculation for ground state and TD-DFT for excited state, immersed in pyridine and *n*-methylformamide-mixture respectively, by means of the Polarizable Continuum Model (PCM). The initial geometry (bond lengths and angles) of the octahedral units was the ideal one, with all bond Cd-Cl equal to 2.868 Å. Relaxed ground and excited states geometries were obtained without any imaginary frequency.The long-range corrected CAM-B3LYP functional[9] was employed with the LANLDZ basis including a pseudopotential for inner electron for Cd and the 6-31+G** basis for Cl and Br.[10–13]

Table S1. Crystallographic data for compounds (TDMP)MCl_4 (M = Cu or Cd).

	(TDMP)$CuCl_4$	**(TDMP)$CdCl_4$**
Space group	*C*2/*c*	*C*2/*c*
a/Å	14.5625(5)	15.2462(10)
b/Å	14.5977(5)	15.1744(9)
c/Å	5.9349(1)	5.7267(2)
α/°	90	90
β/°	107.284(2)	105.733(4)
γ/°	90	90
Radiation	Mo Kα	Mo Kα
2*Θ* range for data collection/°	13 to 57.18	12.84 to 54.18
Reflections collected	12984	11969
Data/restraints/parameters	1519/0/61	1393/0/60
Goodness-of-fit on F^2	1.042	1.033
Final R indexes [$I \geq 2\sigma(I)$]	R_1 = 0.0305 wR_2 = 0.0998	R_1 = 0.0265 wR_2 = 0.0757
Largest diff. peak/hole / e $Å^{-3}$	0.85/-0.40	0.88/-0.47

Table S2. Comparison of bond lengths (Å) of TDMP in the salt (TDMP)Cl_2,[14] and (TDMP)$CdCl_4$.

	$(TDMP)Cl_2$	**$(TDMP)CdCl_4$**
C_{methyl}-C_{cycle1}	1.5151(9)	1.5087(27)
C_{cycle1}-C_{cycle2}	1.5346(17)	1.5105(24)
C_{cycle1}-N_{cycle}	1.5026(8)	1.5000(24)
C_{cycle2}-N_{cycle}	1.5063(9)	1.4857(23)

Table S3. Atomic positions for $(TDMP)CuCl_4$.

Atoms	*x/a*	*y/b*	*z/c*
C2	0.34885(9)	0.25157(10)	0.6387(2)
C3	0.36523(13)	0.40903(11)	0.4962(4)
C4	0.31071(9)	0.32021(9)	0.4429(2)
Cl1	0.33014(2)	0.08833(2)	0.11949(5)
Cl2	0.5	-0.06741(3)	0.25
Cl3	0.5	0.24315(3)	0.25
Cu1	0.5	0.08853(2)	0.25
H1A	0.3169	0.12609	0.71207
H1B	0.30152	0.13809	0.46277
H2A	0.41599	0.23925	0.65523
H2B	0.34496	0.27736	0.78622
H3A	0.33411	0.45412	0.38106
H3B	0.36653	0.42988	0.65055
H3C	0.42984	0.3998	0.49105
H4	0.31852	0.29491	0.29678
N1	0.29384(7)	0.16421(8)	0.59146(19)

Table S4. Atomic positions for (TDMP)$CuCl_4$.

Atoms	*x/a*	*y/b*	*z/c*
C2	0.15803(12)	0.25154(12)	-0.1503(3)
C3	0.31017(12)	0.18150(12)	-0.0500(3)
C4	0.36035(16)	0.09537(13)	0.0142(5)
Cd1	0	0.09457(2)	0.25
Cl1	0	0.07748(3)	-0.25
Cl2	0.17741(3)	0.08773(3)	0.38394(7)
Cl3	0	0.25817(4)	0.25
H1A	0.19008	0.13035	-0.21749
H1B	0.19882	0.14331	0.03679
H2A	0.16568	0.27553	-0.30056
H2B	0.09368	0.23993	-0.17335
H3	0.32185	0.2046	-0.19849
H4A	0.35577	0.07588	0.16994
H4B	0.42332	0.10349	0.01967
H4C	0.33389	0.05193	-0.10618
N1	0.20958(10)	0.16758(9)	-0.0942(3)

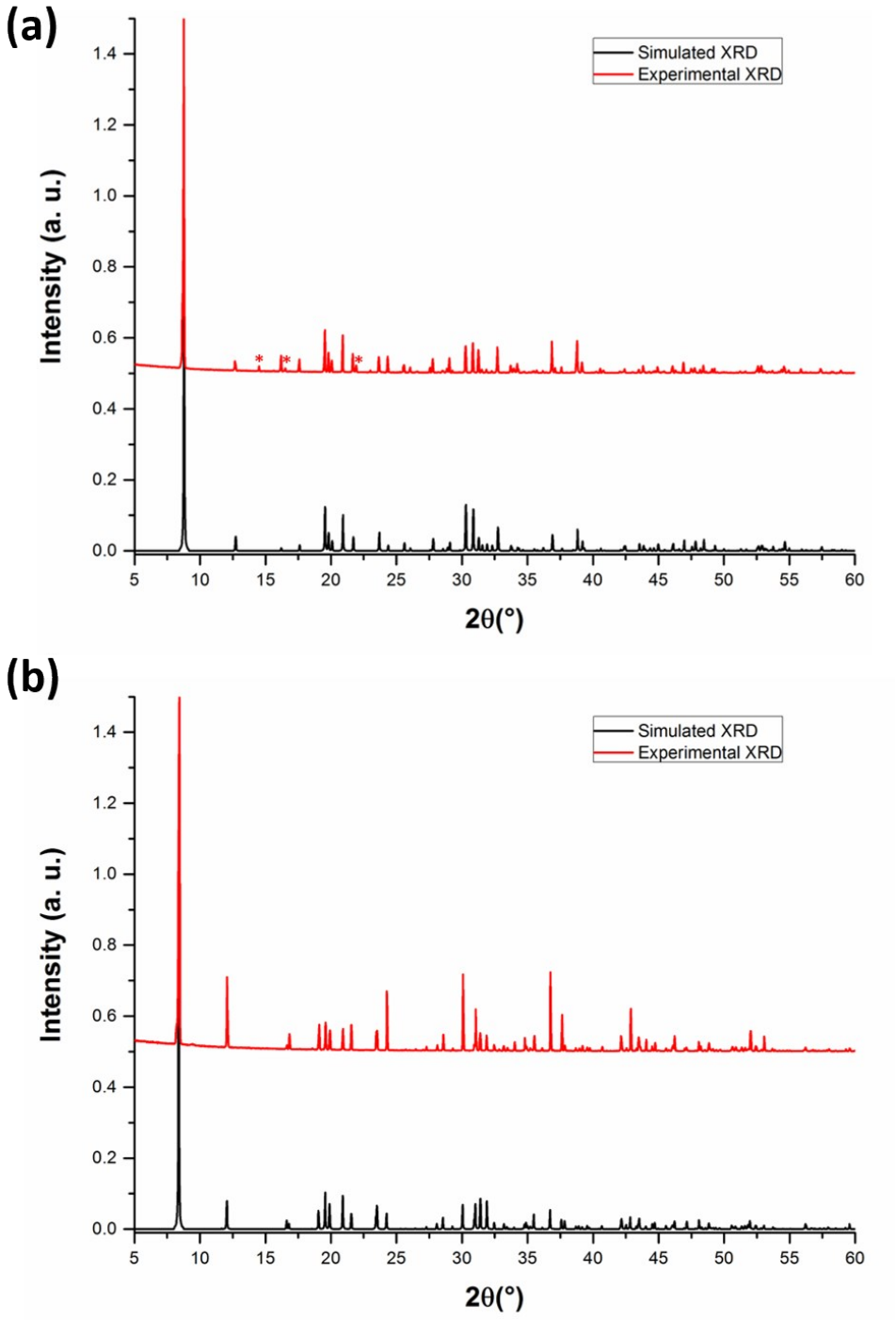

Figure S1. Powder X-ray diffraction patterns of (a) $(TDMP)CuCl_4$ (red asterisk: unknown impurity phase) and (b) $(TDMP)CdCl_4$ at room temperature.

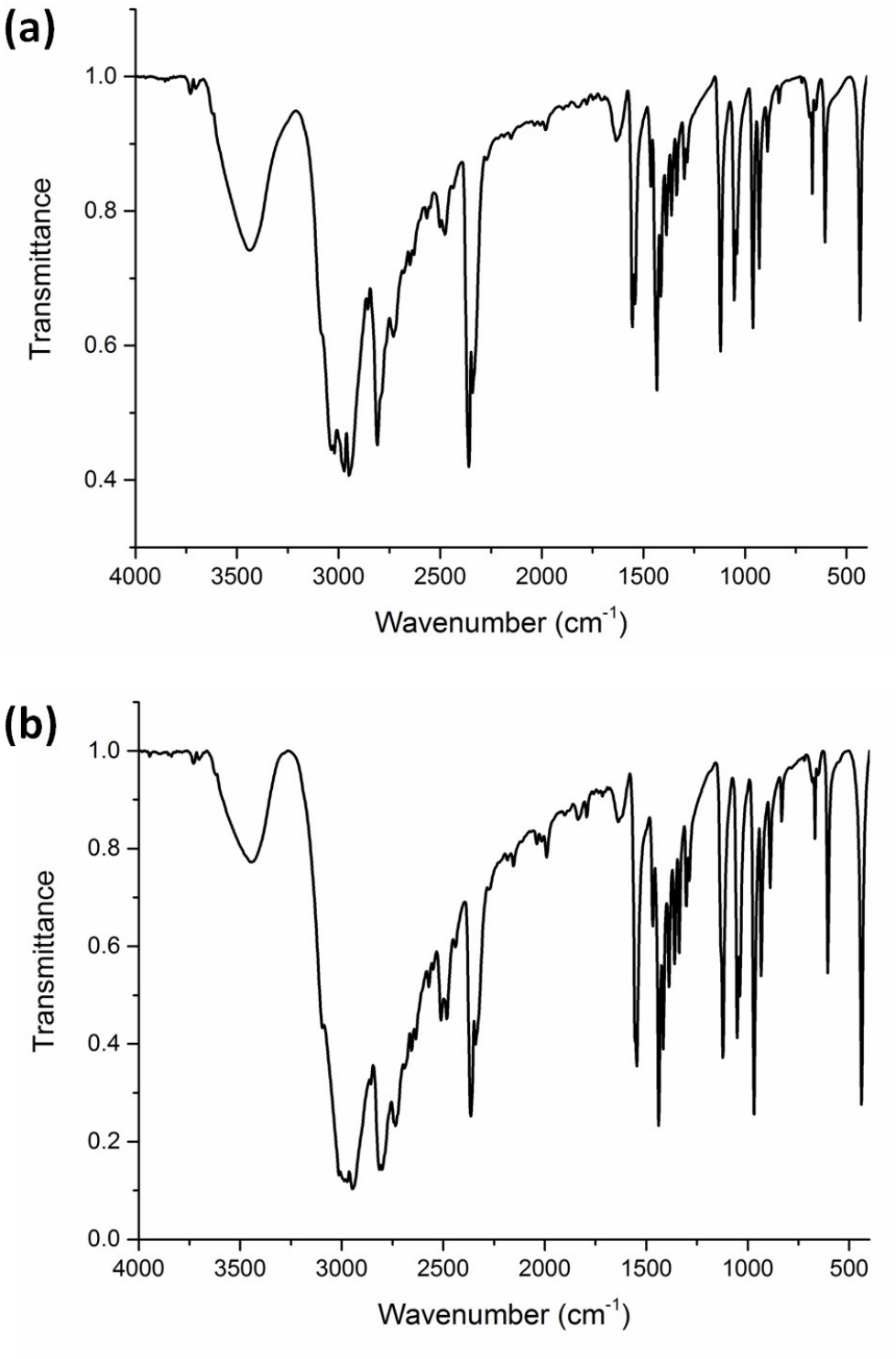

Figure S2. FTIR spectra of (a) $(TDMP)CuCl_4$ and (b) $(TDMP)CdCl_4$ at room temperature.

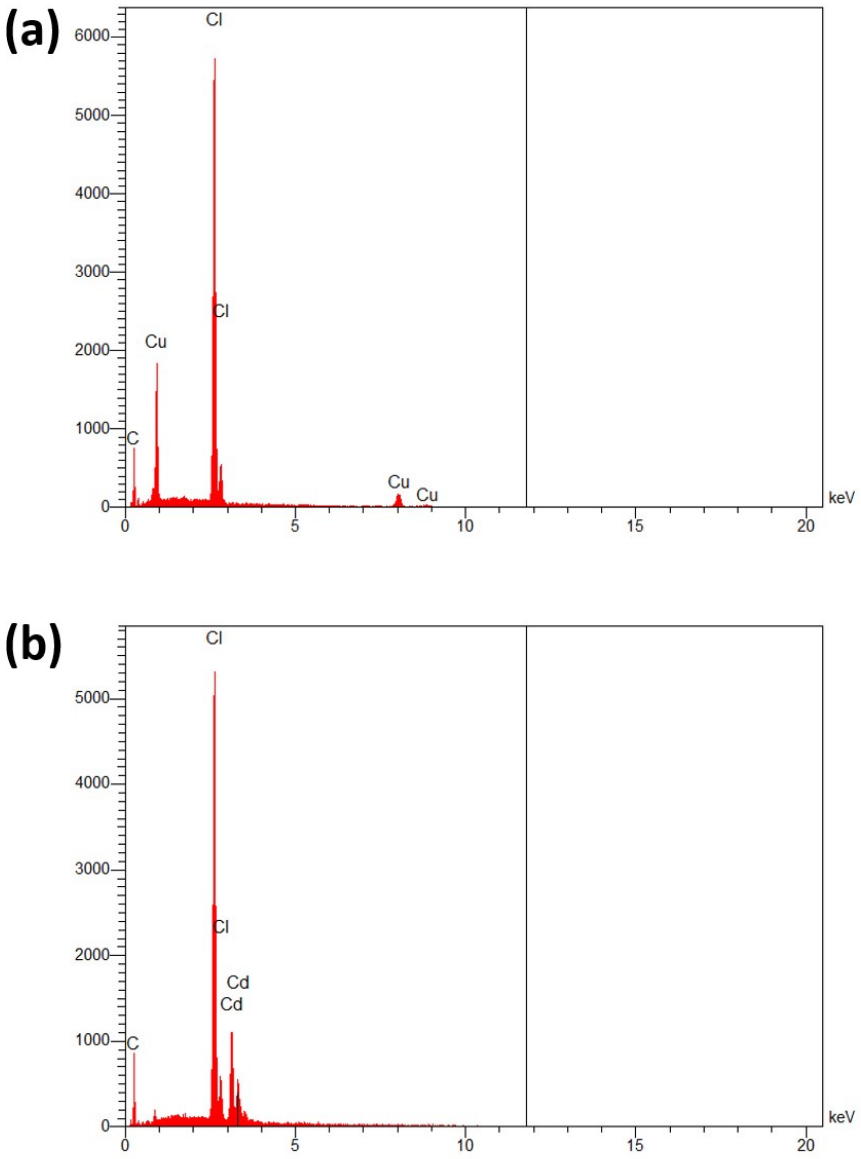

Figure S3. EDX analysis of (a) (TDMP)$CuCl_4$ (Ratio 1/4.3 for Cu /Cl) and (b) (TDMP)$CdCl_4$ (Ratio 1/4.0 for Cd/Cl).

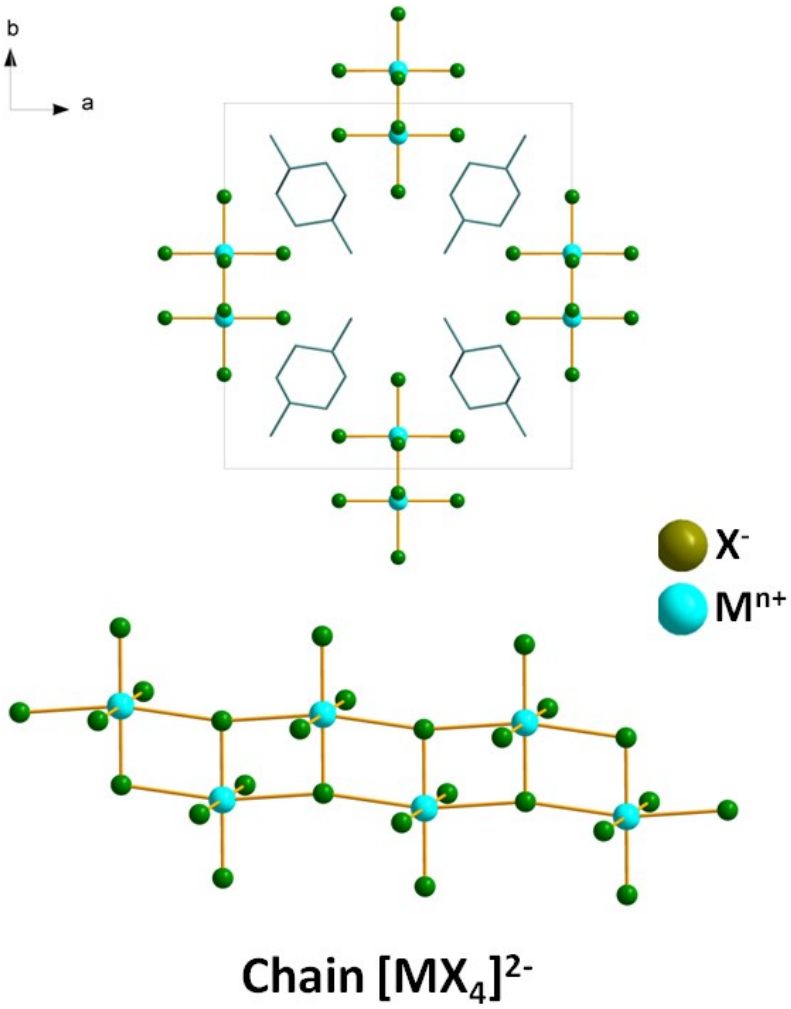

Figure S4. Representations of the metal chloride ladders in the crystal structures of $(TDMP)CuCl_4$ and $(TDMP)CdCl_4$.

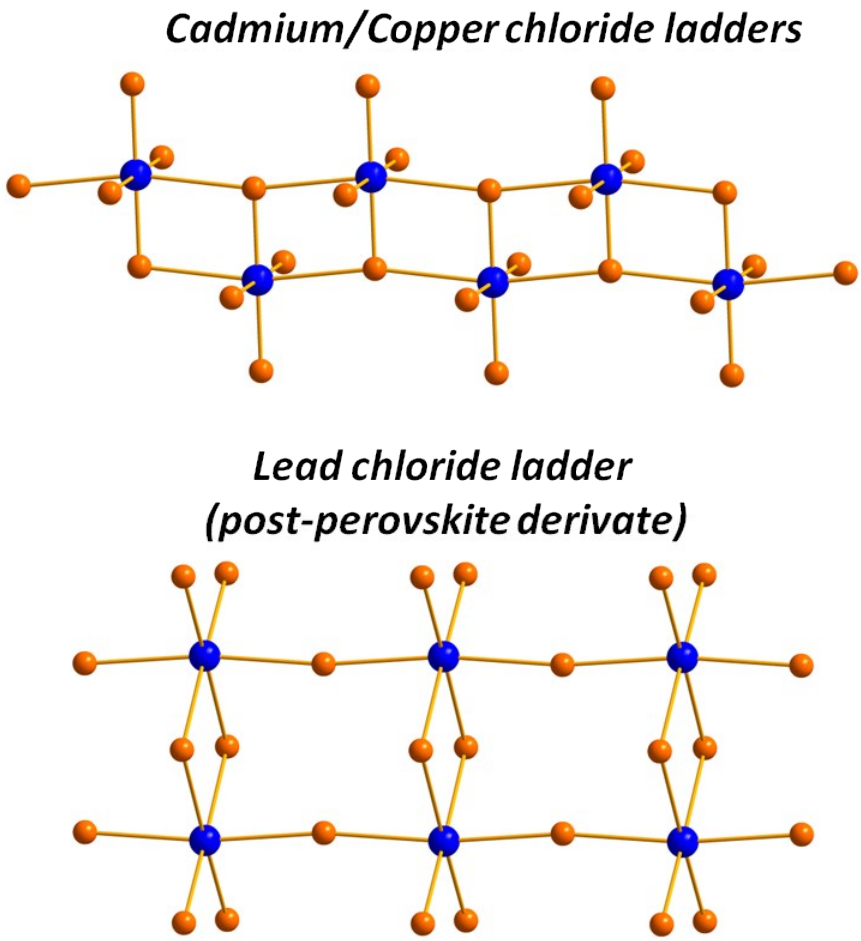

Figure S5. Comparison of the ladders structure of cadmium/copper vs. lead chloride compounds.

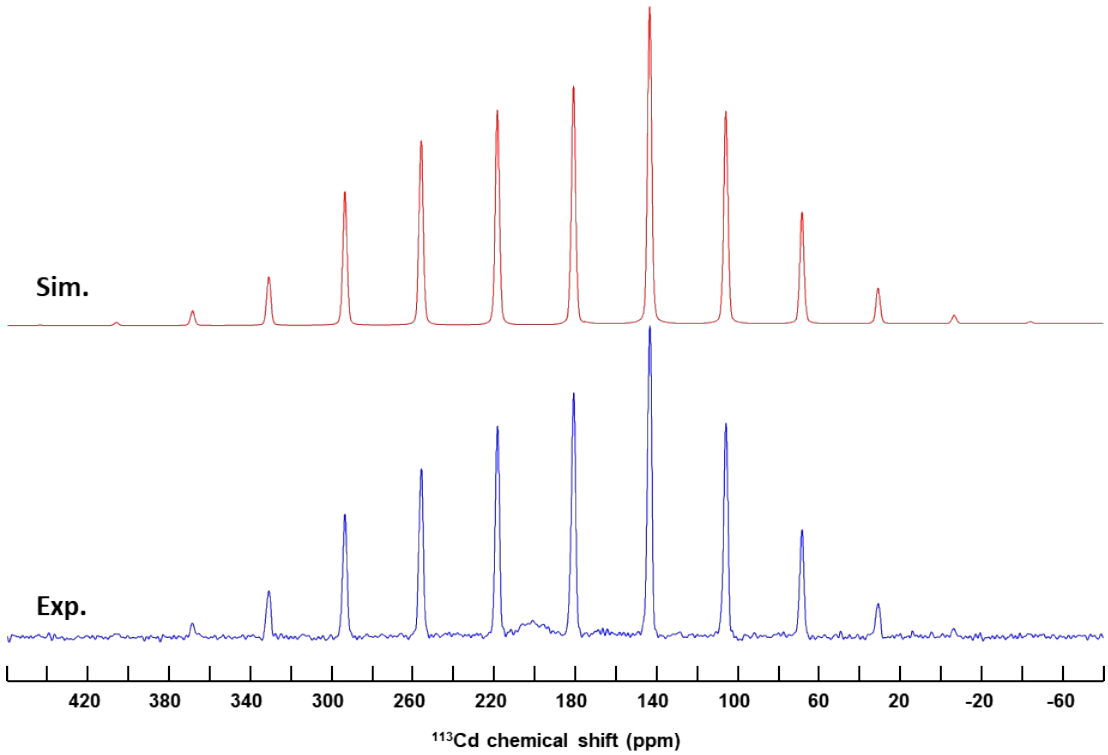

Figure S6. ^{1}H-^{113}Cd CP-MAS (2.5 kHz) NMR spectrum of (TDMP)$CdCl_4$ and its simulation by a single line at 181 ppm. The chemical shift anisotropy is 157 ppm and the asymmetry parameter is 0.79. The weak and broad line at ~200 ppm is attributed to a low amount of cadmium chloride impurity.

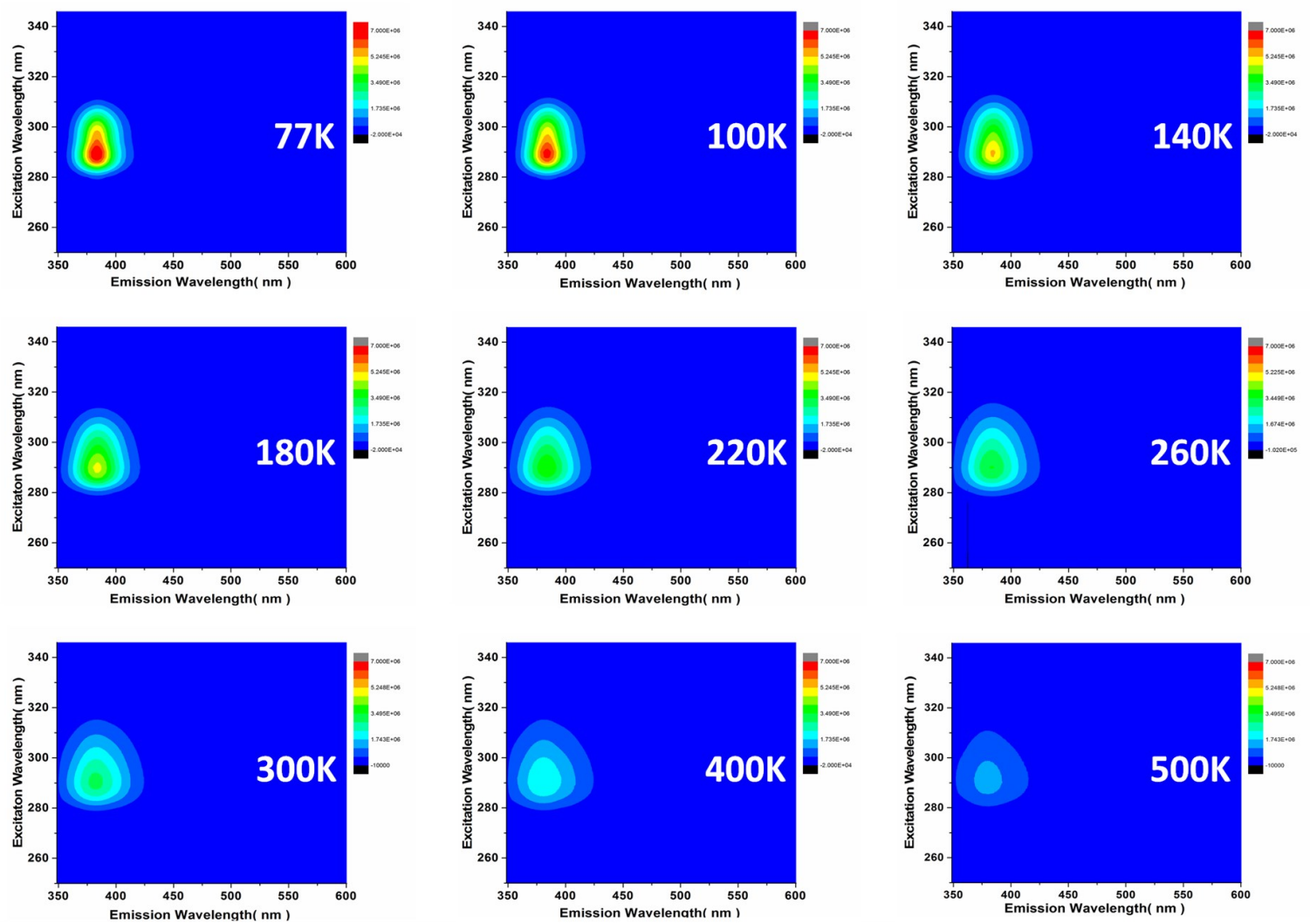

Figure S7. Temperature dependent photoluminescence mapping of (TDMP)$CdCl_4$.

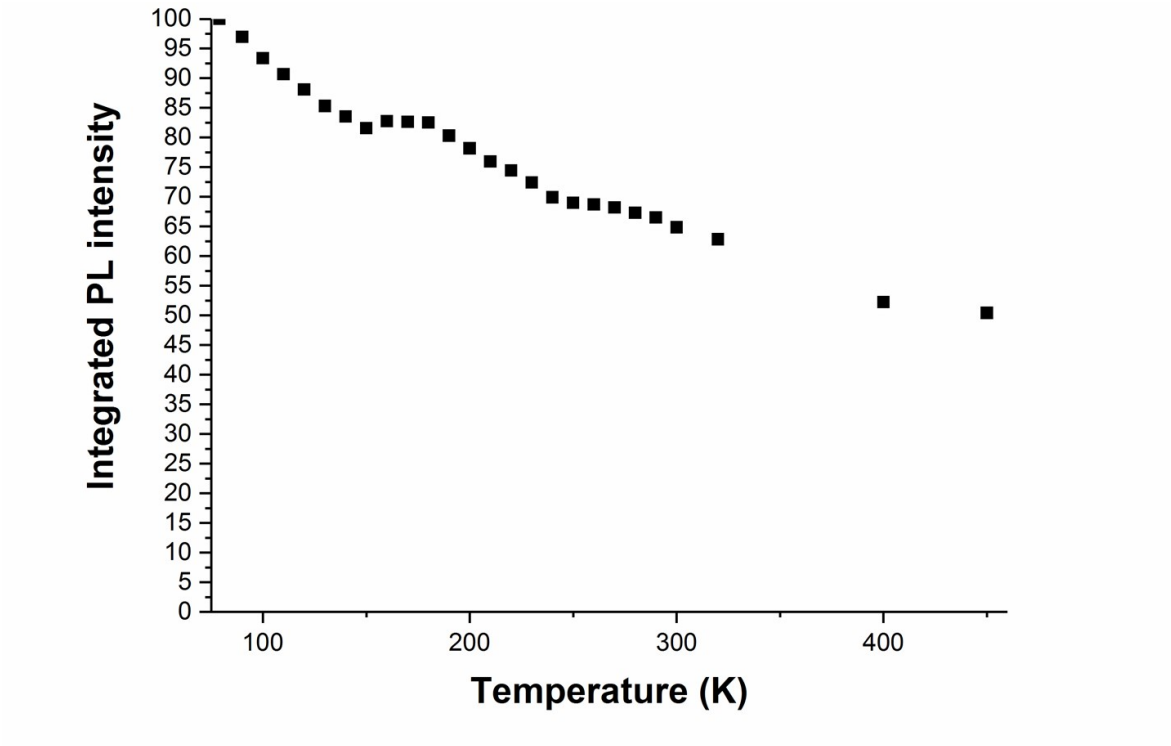

Figure S8. Evolution of PL intensity integrated between 348 and 600 nm with temperature for (TDMP)$CdCl_4$.

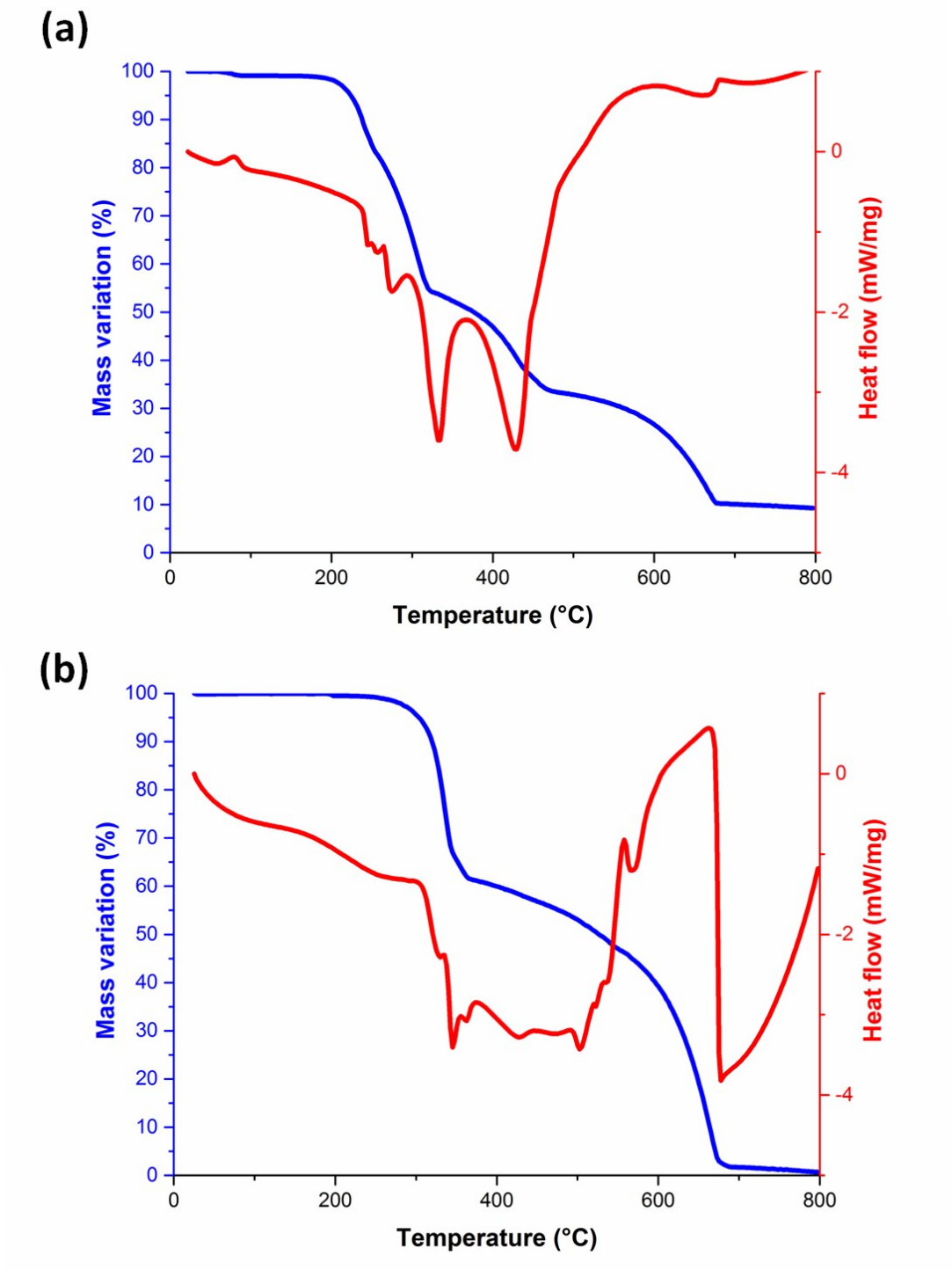

Figure S9. Thermal analysis of (a) $(TDMP)CuCl_4$ and (b) $(TDMP)CdCl_4$ under air.

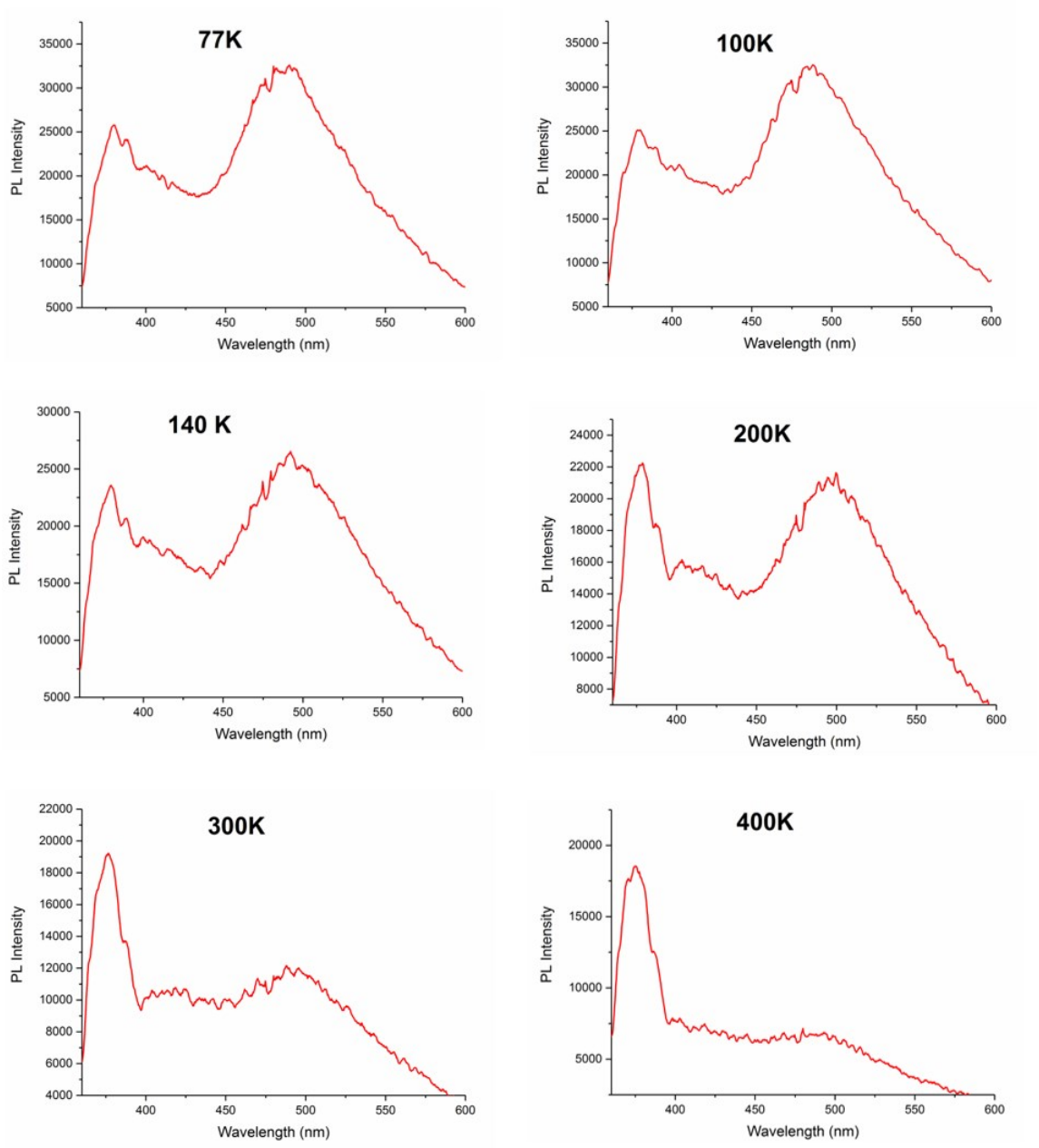

Figure S10. Evolution of the yellow emission of $(TDMP)CdCl_4$ with temperature (λ_{exc} = 346 nm).

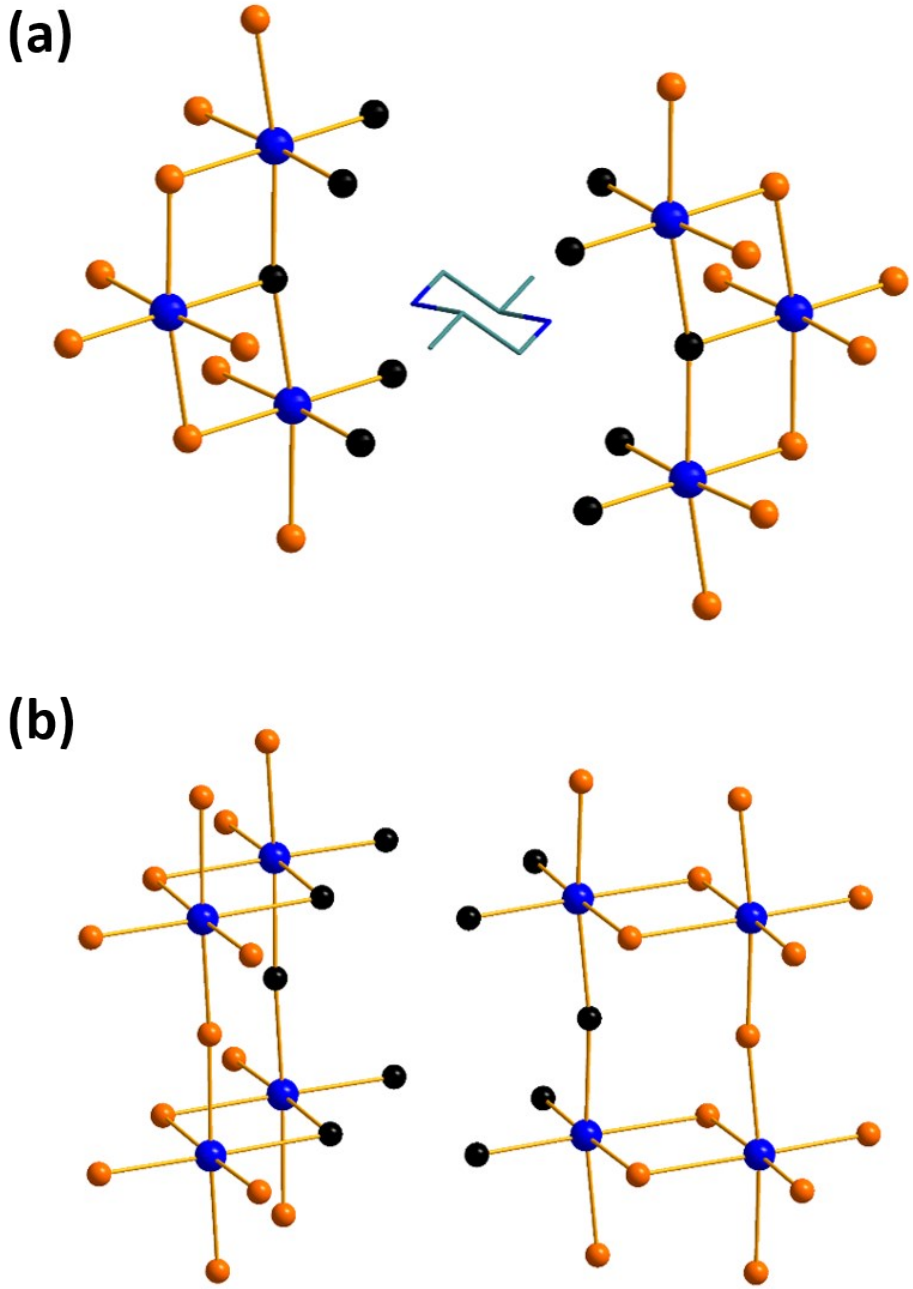

Figure S11. Local environments of the $TDMP^{2+}$ cations for (a) $(TDMP)CdCl_4$, and (b) $(TDMP)PbCl_4$ (For this compound, $TDMP^{2+}$ cannot be localized by X-ray diffraction but solid-state NMR suggest a localization between the ten halide ions highlighted in black).

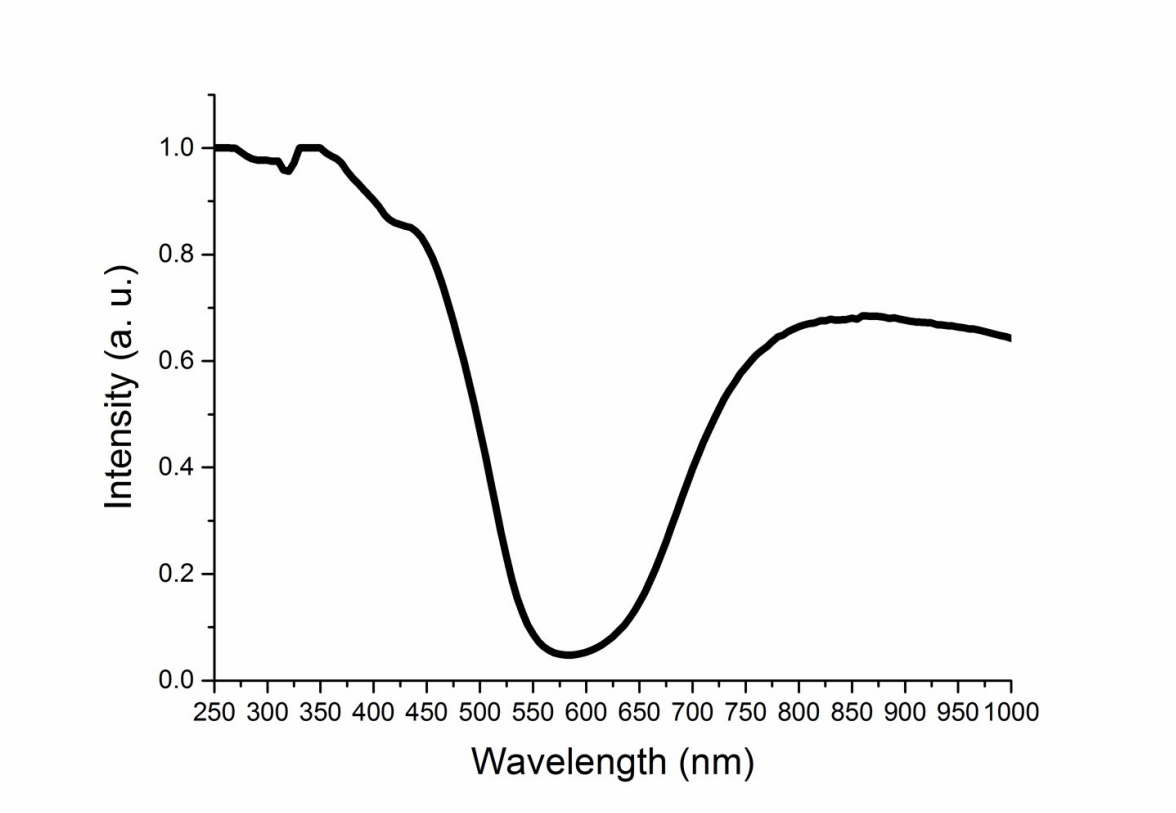

Figure S12. Kubelka-Munk spectra of (TDMP)$CuCl_4$ at room temperature.

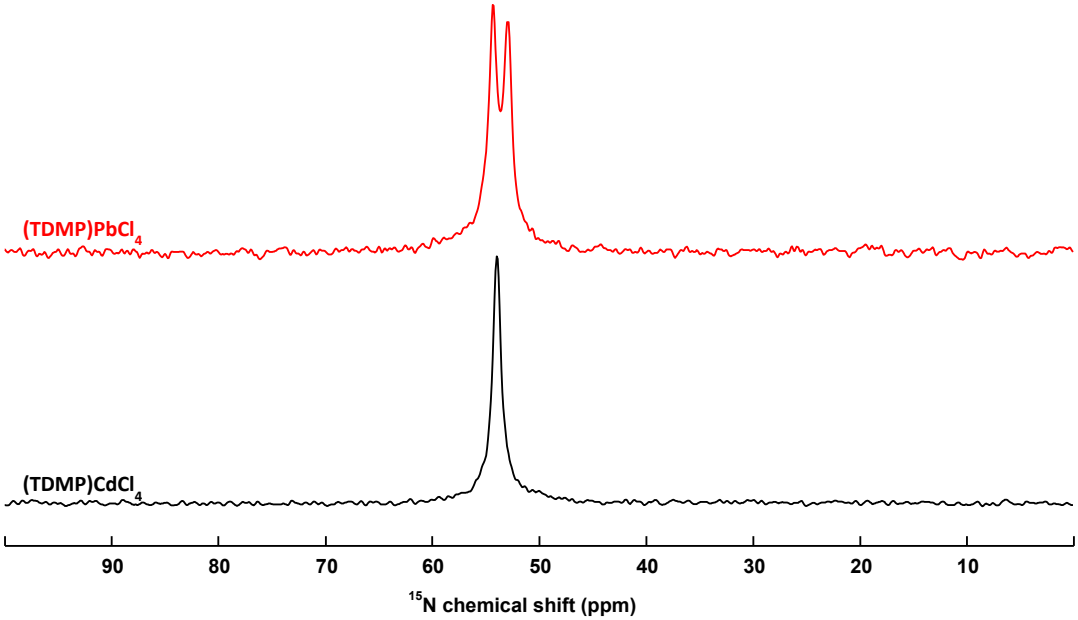

Figure S13. ^{1}H-^{15}N CP-MAS NMR spectra of $(TDMP)CdCl_4$ and $(TDMP)PbCl_4$. $(TDMP)CdCl_4$ exhibits a single line at 54 ppm whereas $(TDMP)PbCl_4$ exhibits two lines. This difference could originate from small differences in the hydrogen bond networks. In $(TDMP)CdCl_4$, the two hydrogen atoms of the NH_2^+ group bond with two bromine atoms belonging to the same crystallographic site. In contrast, in the case of $(TDMP)PbCl_4$, the two bromine atoms belong to two different crystallographic sites.

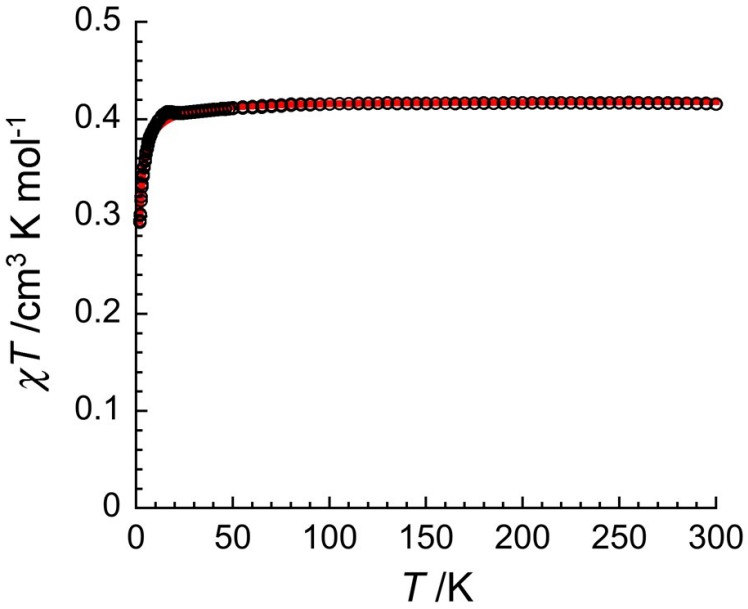

Figure S14. Temperature dependence of the χT product (where χ is the molar magnetic susceptibility that equals M/H per mole of (TDMP)$CuCl_4$) collected in an applied dc magnetic field of 0.1 T. The solid line is the best fit considering a quantum S = ½ spin chain model (see text),

REFERENCES

(1) Sheldrick, G. M. *SADABS*; University of Göttingen: Germany, 2002.
(2) Burla, M. C.; Caliandro, R.; Camalli, M.; Carrozzini, B.; Cascarano, G. L.; De Caro, L.; Giacovazzo, C.; Polidori, G.; Spagna, R. SIR2004: An Improved Tool for Crystal Structure Determination and Refinement. *J. Appl. Crystallogr.* **2005**, *38* (2), 381–388. https://doi.org/10.1107/S002188980403225X.
(3) Sheldrick, G. M. Crystal Structure Refinement with SHELXL. *Acta Crystallogr. Sect. C Struct. Chem.* **2015**, *71* (1), 3–8. https://doi.org/10.1107/S2053229614024218.
(4) Dolomanov, O. V.; Bourhis, L. J.; Gildea, R. J.; Howard, J. A. K.; Puschmann, H. OLEX2 : A Complete Structure Solution, Refinement and Analysis Program. *J. Appl. Crystallogr.* **2009**, *42* (2), 339–341. https://doi.org/10.1107/S0021889808042726.
(5) Spek, A. L. *PLATON ; Utrecht University: Utrecht, The Netherlands, 2001*.
(6) Massiot, D.; Fayon, F.; Capron, M.; King, I.; Le Calvé, S.; Alonso, B.; Durand, J.-O.; Bujoli, B.; Gan, Z.; Hoatson, G. Modelling One- and Two-Dimensional Solid-State NMR Spectra. *Magn. Reson. Chem.* **2002**, *40* (1), 70–76. https://doi.org/10.1002/mrc.984.
(7) Kersen, Ü.; Wojtczak, A.; Bienko, A.; Jezierska, J. The Effects of Protonated Heterocyclic Cations on the Structural and Magnetic Properties of Tetrachlorocuprate(II) Anions; X-Ray, Magnetochemical and EPR Studies. *New J. Chem.* **2018**, *42* (19), 15705–15713. https://doi.org/10.1039/C8NJ03155J.
(8) Frisch, M. *Gaussian, Inc., Wallingford CT, 2016. Gaussian G16A03.*; 2016.
(9) Yanai, T.; Tew, D. P.; Handy, N. C. A New Hybrid Exchange–Correlation Functional Using the Coulomb-Attenuating Method (CAM-B3LYP). *Chem. Phys. Lett.* **2004**, *393* (1), 51–57. https://doi.org/10.1016/j.cplett.2004.06.011.
(10) Dunning, Thom. H.; Hay, P. J. Gaussian Basis Sets for Molecular Calculations. In *Methods of Electronic Structure Theory*; Schaefer, H. F., Ed.; Modern Theoretical Chemistry; Springer US: Boston, MA, 1977; pp 1–27. https://doi.org/10.1007/978-1-4757-0887-5_1.
(11) Hay, P. J.; Wadt, W. R. Ab Initio Effective Core Potentials for Molecular Calculations. Potentials for the Transition Metal Atoms Sc to Hg. *J. Chem. Phys.* **1985**, *82* (1), 270–283. https://doi.org/10.1063/1.448799.
(12) Hay, P. J.; Wadt, W. R. Ab Initio Effective Core Potentials for Molecular Calculations. Potentials for K to Au Including the Outermost Core Orbitals. *J. Chem. Phys.* **1985**, *82* (1), 299–310. https://doi.org/10.1063/1.448975.
(13) Wadt, W. R.; Hay, P. J. Ab Initio Effective Core Potentials for Molecular Calculations. Potentials for Main Group Elements Na to Bi. *J. Chem. Phys.* **1985**, *82* (1), 284–298. https://doi.org/10.1063/1.448800.
(14) Bart, J. C. J.; Bassi, I. W.; Scordamaglia, R. The Crystal Structure and Molecular Conformation of Trans-2,5-Dimethylpiperazine Dihydrochloride. *Acta Crystallogr. B* **1978**, *34* (9), 2760–2764. https://doi.org/10.1107/S0567740878009176.